Helium apparent diffusion coefficient and trapping mechanisms in implanted B_4C boron carbide

Vianney Motte, Dominique Gosset, Thierry Sauvage, Hélène Lecoq, Nathalie Moncoffre

Helium apparent diffusion coefficient and trapping mechanisms in implanted B_4C boron carbide

Vianney Motte[1-3], Dominique Gosset[1], Thierry Sauvage[2], Hélène Lecoq[2], Nathalie Moncoffre[3]

[1] *DEN-Service de Recherche de Métallurgie Appliquée, CEA, Université Paris-Saclay, 91191 Gif-sur-Yvette, France*

[2] *CNRS, CEMHTI, Orléans, 45071 Orléans, France*

[3] *Université de Lyon, Université Lyon 1, CNRS/IN2P3, IPNL - UMR 5822, F-69622, LYON, France*

Abstract

When boron carbide is irradiated in nuclear reactors, large helium quantities are produced due to the (n,α) neutron absorption reactions. In a recent paper, we have identified the trapping sites for helium, grain boundaries and damaged zones. In this paper, we propose the determination of an apparent diffusion coefficient for helium. ^{3}He implantations then annealing were performed in B_4C samples of different grain sizes. The $^3He(^2H,\alpha)^1H$ nuclear reaction was used to profile helium before and after annealing. Helium profiles with two superimposed components were observed. The narrow component is attributed to helium trapped in the implanted, damaged zone, either in clusters too small to be seen by TEM or as helium-defect complexes. The large component evolution is bounded by the distribution of the grain boundaries surrounding the implanted zone, confirming the high trapping efficiency of the grain boundaries. From an Arrhenius plot, an activation energy for helium diffusion in grains of 2.0 ± 0.2 eV was deduced in a large grain size material.

Keywords

Boron carbide, helium diffusion, nuclear reaction analysis, transmission electron microscopy

1 Introduction

Because of a high neutron absorption cross section of the boron-10 isotope, a high melting temperature (2450°C), a good resistance under irradiation and a relatively low cost, boron carbide appears as a key material to control the power of nearly all types of nuclear power plants [1]. Its crystalline structure is well known [2,3,4]: icosahedra, most often with a ($B_{11}C$) composition, are connected into a rhombohedral network with a central chain along the main diagonal of the

rhombohedra with a most probable C-B-C composition; this leads to a mean composition close to B_4C .

Under neutron irradiation at high temperature, amorphisation of boron carbide has never been observed. However, recent studies [5,6,7] have shown that amorphisation can occur under ion implantation at and below room temperature when the damage reaches about 8 dpa (displacements per atom). In addition, neutron irradiation produces large quantities of helium due to (n,α) absorption reactions on boron-10. Above 500°C, most observations show helium accumulates as highly pressurised bubbles that lead to swelling and microcracking [8,9,10,11,12,13,14].

In order to avoid the difficulties associated with neutron irradiation, we have studied the behaviour of helium clusters that form after ion implantation and annealing in implanted boron carbide [15]. Increasing post-implantation annealing temperature from 500°C to 1500°C, different clusters form in the implanted zone: nanometric spherical bubbles, lenticular agglomerates of nanometric bubbles, platelets along the (111) or (001) rhombohedral planes, tri-dimension facetted bubbles. Dual-beam implantations, leading to a helium upon atom displacement ratio of about 1/200, similar to fast neutron irradiation [16], have been performed. They show a higher cluster density in the implanted zone as compared to the single beam implantation. These observations are in agreement with those performed on material irradiated in a fast neutron reactor [17]. We have also shown helium clusters only form in the grain boundaries and in the damaged zones (Figure 1). In fact, it appears that helium bubbles nucleate only in damaged or faulted zones.

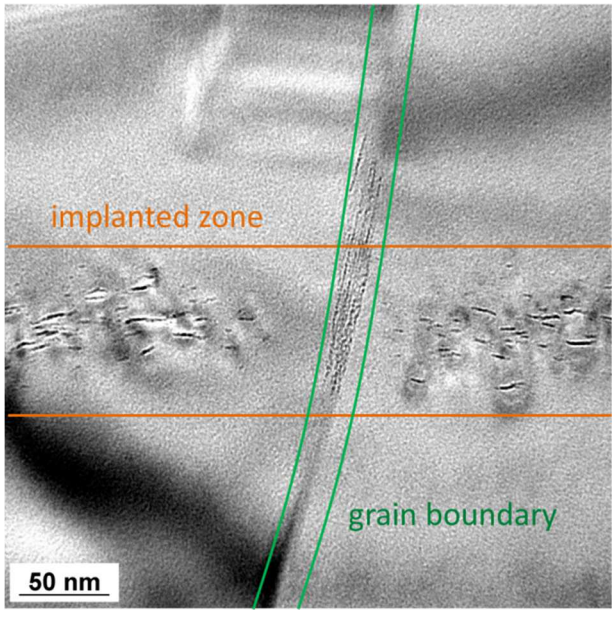

Figure 1: TEM micrograph of helium implanted boron carbide ($10^{16}cm^{-2}$, peak concentration $6.10^{20}/cm^3$) at room temperature and annealed at 700°C for 1 h [15].

However, helium behaviour in boron carbide has been studied mostly in fast neutron irradiated samples. In these conditions, the effect of the different parameters that could influence the

behaviour of the gas can be hardly identified. Therefore, the helium diffusion mechanisms and parameters are not well known. Clayton *et al.* [18] have irradiated high density B_4C samples in the BNLR (Brookhaven National Laboratory Research) reactor at low temperature, possibly in a thermal neutron flux. The ^{10}B burnup is estimated about 0.05 at.% (i.e. about $5x10^{19}$ cm^{-3}). They estimated a diffusion coefficient from helium release measurements during post-irradiation annealing. The classical expression $D = D_0 \exp(-E_a/kT)$ was used, with E_a(activation energy) equal to 1.26 eV and D_0 (pre-exponential factor incorporating the diffusion mechanism yield and frequency) equal to $4.4x10^{-9}$ $cm^2.s^{-1}$. Similar analyses were performed by Hollenberg from 92% density boron carbide samples irradiated at low fluence (burnup $5x10^{20}$ cm^{-3}, i.e. ~0.4 at.%) and high temperatures (630 – 950°C) in the EBR-II fast neutron reactor in sealed capsules [19]. It is worth noting that the fast neutron scattering induces a high atom displacement rate. Slightly different diffusion coefficients were derived, with Ea = 1.46 eV and $D_0 = 1.40x10^{-8}$ cm^2 s^{-1}. But those values correspond to helium diffusion in materials that have been irradiated at different temperatures,, burnups and for different neutron spectra. Moreover, integral methods are used: annealing is performed on as-irradiated samples. The values are then probably biased because of interactions with irradiation damage, helium clusters or grain boundaries. Kovyrshin [20] has irradiated boron carbide powders of different grain sizes in a VVR-M reactor (water-cooled reactor, thermal neutron fluences from $1.2x10^{19}$ to $9x10^{19}$ cm^{-2}) at low temperature. In those conditions, the structural damage arises only from the slowing down of the He and Li resulting from the neutron absorption reaction. After thermo-desorption experiments, the author observed different release steps which analysis leads to different activation energies, 0.3±0.1 eV (attributed to grain surface desorption), 1.2±0.2 eV and 2.3±0.3 eV. A nearly complete helium release was obtained after heating at 1050°C. Re-analysing those data with a different physico-mathematical model, Svetukhin [21] obtained quite different and very low diffusion energies (~0.7 eV). Nevertheless, it seems that the migration energy of helium is much lower than the B or C interstitial ones, about 3 to 4.5 eV [22]. It can be then inferred that the migration of free helium will occur at much lower temperature than the healing of the structural damage, which arises around 1200 – 1500°C [23].

On the other hand, Schneider *et al.* have simulated helium behaviour by DFT calculations [24]. They first determined the most likely interstitial sites for helium. Two different sites were found, respectively located around (6 sites “2”) and above (2 sites “3”) the central chain. The migration of helium was then studied with the NEB (Nudged Elastic Band) method. Three migration paths were identified between the two most likely interstitial sites, respectively between two sites “2” in a given cell (type “A”), between site “2” and site “3” of adjacent cells (type “B”) and between two sites “3” of adjacent cells (type “C”).From those migration paths, it was deduced that two kinds of migration exist:

- A 2D migration: combination of types A and B with an energy barrier of 1.2 eV, leading to a planar diffusion in the (111) plane of the rhombohedral structure.
- A 3D migration: combination of types B and C and an energy barrier of 2.2 eV.

Very similar results were recently obtained by [22]. Those values are thus very close to the ones determined by Kovyrshin. However, the issue with the present DFT calculations is that they consider one single helium atom in a B_4C cell without neither point defect nor electron charge effect. In irradiated boron carbide, the material has undergone neutron damage leading to a high density of point defects (about 300 defects per created helium in a fast neutron flux [16]) and helium atoms that have been created can agglomerate. Hence, it is difficult to compare those results.

In that context, we have launched a parametric study to determine the parameters that influence the behaviour of implanted helium. In this paper, an apparent diffusion coefficient is determined and the diffusion mechanisms of helium are discussed.

2 Experiments

2.1 Experimental procedure

Pure B_4C powders of different grain sizes were sintered either by hot pressing or by SPS (Spark Plasma Sintering) leading to small grain size (0.3-1 µm), medium grain size (1-6 µm) and large grain size (20-60 µm) materials. The large grain size material is intended to determine the apparent helium diffusion coefficient. The small and medium size materials allow studying the influence of the microstructure. The two sintering processes lead to cylindrical pellets with nearly fully dense materials (over 98% of the theoretical density: Figure 2). The B_4C pellets were then cut and polished with diamond pastes until the material is mirror-polished. As boron carbide is a very hard material, the polishing steps induce a high density of mechanical defects up to depths of about 500 nm that could interfere with the implanted helium. To heal those defects or reduce their density, subsequent annealing at 1600°C (i.e. close the admitted ductile-brittle temperature threshold) for 3 h was performed.

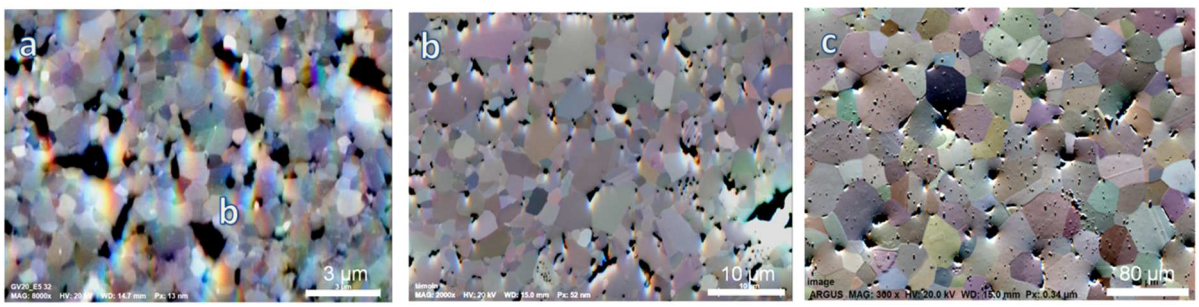

Figure 2: FSE ESM micrographs of boron carbide sintered with different powders. a) small grain size (0.3-1 µm); b) medium grain size(1-6 µm); c) large grain size (20-60 µm). Densities are over 98%, most of the porosities correspond to grain pulling out during polishing.

Helium ions were then implanted at different fluences in the discs. This allows controlling some key parameters such as the He concentration, the implanted range and depth and the temperature. Moreover, irradiation defects, whose consequence on diffusion could be important, are produced during helium implantation at relatively low concentration as compared to fast neutron irradiation (see here under). Subsequent annealing was then performed. The heating and (initial) cooling rates were 100°C/min. Different samples were used for each implantation and annealing condition. This is required since low temperature mechanisms could influence the high temperature ones: see discussion (e.g., clusters nucleation, helium-defects complexes dissociation…).

The study was carried out using two main techniques:

- NRA (Nuclear Reaction Analysis), which is a well-known ion beam analysis technique widely used to profile helium [25,26]. For this purpose, ^{3}He implantations were performed on the DIADDHEM (CNRS-Orléans, France) facility [27].
- TEM (Transmission Electron Microscopy), to observe helium clusters. For these experiments, ^{4}He implanted B_4C samples were prepared at the JANNUS (CEA-Saclay, France) facility [28].

A synthesis of the experimental conditions as a function of the probing technique is presented in Table 1.

Table 1. Summary of the experiments.

Initial powder	ERM		HP	HD20	
Grain size µm	20 - 50		1 - 6	0.3 – 1.0	
Analysis	NRA	TEM	NRA	NRA	TEM
Objective	Apparent diffusion coefficient	Fluence threshold for bubbles in implanted zone	He profile vs microstructure and annealing conditions		He bubbles distribution
Ion	^{3}He	^{3}He	^{3}He	^{3}He	^{4}He
Energy (keV)	1200	1200	1200	1200	500
Ion beam incidence (°)	60	60	60	60	15
Range (µm)	1.37	1.37	1.37	1.37	1.21
Straggling (µm)	0.073	0.073	0.073	0.073	0.054*
Fluence /10^{15}.cm²	2	2 – 4	2	2	8
Max. He c° /10^{20}.cm^3	1	1 – 2	1	1	5.5
at.%	0.07	0.07 – 0.14	0.07	0.07	0.40
Annealing °C	600 – 800	800	600 – 1000	800	800
h	1 – 3	1	1 – 10	1	1

** the different stragglings come from different implantation angles. This results in different fluence over maximum concentration ratio.*

2.2 Helium profiling by using the $^{3}He(^{2}H,\alpha)H$ nuclear reaction

^{3}He in-depth profiling was obtained thanks to the $^{3}He(^{2}H,^{4}He)^{1}H$ nuclear reaction. Hence, the ^{3}He isotope was implanted to simulate the presence of helium in B_4C. The ^{3}He in-depth distribution was deduced from the ^{4}He energy spectrum. The apparent helium diffusion coefficients in B_4C were then determined from the ^{3}He depth profile evolution as a function of annealing conditions, temperature and time.

The basic principle of this analysis is the following: deuterons impinge the sample and ^{4}He particles emitted from the nuclear reaction are detected by a PIPS annular detector placed at 178° from the beam direction and at a distance of 104 mm from the sample surface (detector surface 100 mm², detection solid angle 6.27 mSr). For a single detection configuration, the ^{4}He signal is convoluted with signals inherent to the presence of parasite nuclear reactions such as (d,p) reactions on boron isotopes. To suppress all interferences in the region of interest of the ^{4}He signal, we used the coincidence technique. Whenever a particle is detected by the 178° detector, the event is recorded if and only if an event is detected by a second detector placed at 0° with a 1200 mm² active surface and at a distance of 60 mm from the rear surface of the sample (detection solid angle 0.27 Sr). For the $^{3}He(^{2}H,^{4}He)^{1}H$ nuclear reaction, the ^{4}He signal is systematically recorded because simultaneously to the ^{4}He particle emission, the kinematic of the reaction induces a proton is emitted in the opposite direction of ^{4}He. The proton energy is high enough (16 MeV) to be transmitted through the 500 µm thick B_4C sample and then detected by the 0° detector. The logic coincidence gate is adjusted to 0.2 µs. The proton signal emitted from the $^{10/11}B(d,p)^{11/12}B$ reactions is rejected because the output of the logic gate is meant to be 0. This coincidence configuration allows reducing the background noise by about 10^4 (Figure 3).

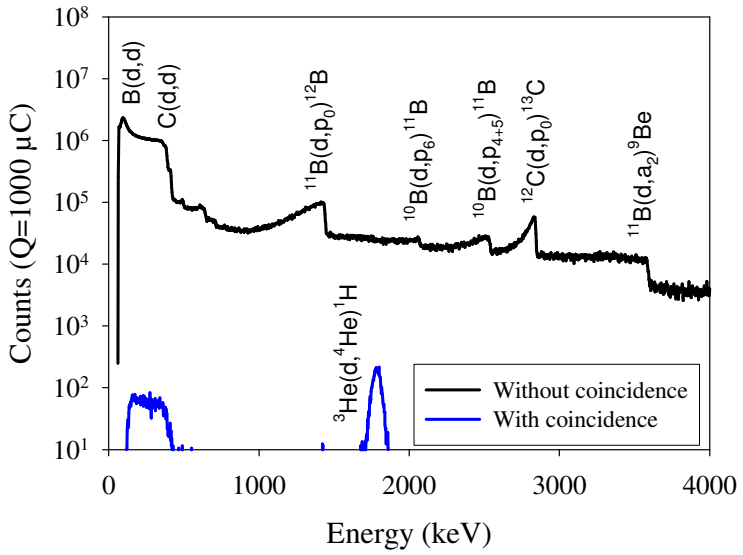

Figure 3. Signals recorded by the 178° annular PIPS detector with (blue line) and without (black line) coincidence for the 2x10^{15} ^{3}He.cm^{-2} as-implanted sample

The ^{3}He incident energy was 1200 keV and the angle from the sample normal was 60°, in order to broaden the reference helium profile over the depth experimental resolution, this increasing the depth resolution. The projected range estimated from the SRIM software [29] is 1.37 µm with a range straggling of 0.087 µm (peak FWHM = 0.20 µm). The range is a compromise chosen first to allow a significant ^{3}He profile broadening before having to take into account surface effects and second to facilitate the FIB-sample preparation for the TEM observations. The implantations of all samples of a given material were simultaneously performed in order to ensure that the fluence is the same for a given analysis. The ^{2}H incident energy for the helium analysis was 800 keV which corresponds to a smooth evolution of the ^{3}He(^{2}H,^{4}He)^{1}H cross section from the surface to about 3 µm depth as shown inFigure 4. It allows a satisfactory compromise between cross section and depth resolution.

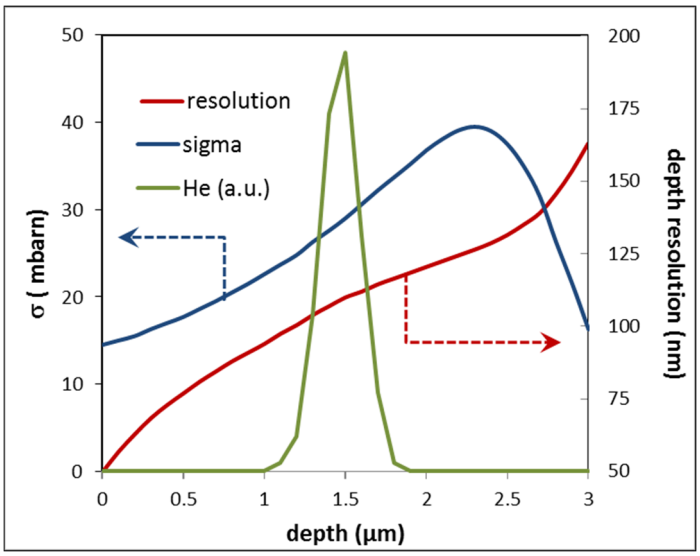

Figure 4: Blue: cross section curve of the ^{3}He(^{2}H,^{4}He)^{1}H reaction for 800 keV deuterons depending on the depth in B_4C. Red: depth resolution for the DIADDHEM CEMHTI facility [27].Green: as-implanted ^{3}He profile (arbitrary units, from SRIM).

The depth resolution was calculated using the RESNRA software. At the projected range (1.37 µm), the depth resolution is close to 0.1 µm, to be compared to the full width at half maximum of about 0.20 µm deduced from SRIM calculation. The calculation and fitting process to determine the helium depth resolution and profile is mentioned in a previous paper [30].

We chose to implant helium at a low fluence (about 2x10^{15} at.cm^{-2}, i.e. about 0.07 He at.% at the maximum of the distribution). This is a good compromise to have a correct detection yield in acceptable experiment duration and to avoid the formation of helium clusters which were observed

above this value by TEM [15] as shown in Figure 5. Two samples were implanted at room temperature at different fluences then annealed at 800°C for 1h: such conditions allow the formation of helium bubbles both in grain boundaries and in the implanted zone. TEM specimens have then been prepared by FIB. At a fluence of $2x10^{15}$ at.cm^{-2} (maximum concentration ~10^{20} at.cm^{-3}), no bubbles are seen in the implanted zone. However, bubbles form in the grain boundaries, as far as 1 µm from the implanted zone, associated with high strain contrasts. At $4x10^{15}$ at.cm^{-2} (maximum concentration ~$2x10^{20}$ at.cm^{-3}), small bubbles form in the implanted zone. However, even if bubbles are not observed in the implanted zone at $2x10^{15}$ cm^{-2}, it should be noted that too small clusters cannot be observed by TEM. On the other hand, SRIM simulations [29] show that each helium atom creates about 50 atom displacements before stopping, mainly in their immediate vicinity (the damage peak is nearly superimposed to the implantation peak: Figure 6): this could perturb the subsequent helium diffusion.

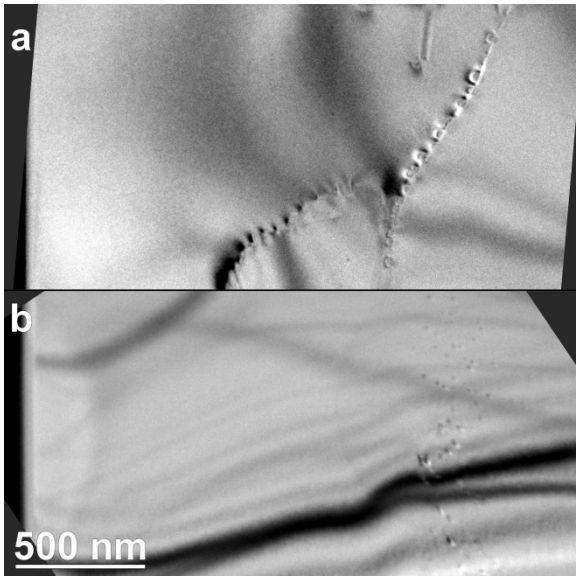

Figure 5. TEM observations of large grain size B_4C implanted with ^{3}He (implantation depth 1.37 µm, surface on the left) then annealed at 800°C 1h. a: $2x10^{15}$at.cm^{-2} (by chance there were grain boundaries in the FIB sample, here decorated with He bubbles). b: $4x10^{15}$ at.cm^{-2}: small bubbles are visible in the implanted band.

The He analysis by NRA was performed at the DIADDHEM facility [27] with a 2x2 mm^2 deuterons beam size and a 60 nA current. The beam charge was modulated to obtain a ^{4}He signal integral higher than 3000 events, necessary to reduce the helium concentration error bars.

An example of ^{3}He profile is shown in Figure 6 and compared with SRIM calculations. The analysed depth differs from the calculated one by about 50 nm, which can be considered as the depth resolution of the method. More importantly, the shapes and the widths of the depth profiles are identical.

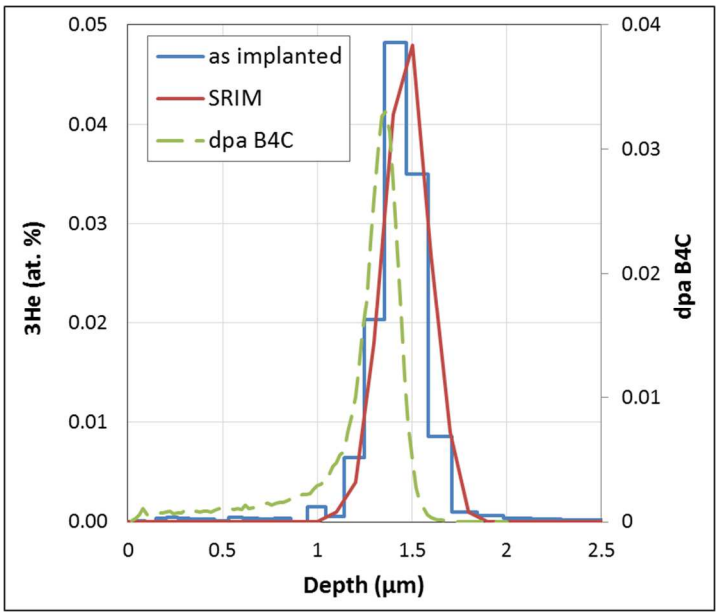

Figure 6: ^{3}He depth profile in boron carbide (1200 keV, 1.6x10^{15} at.cm^{-2}, room temperature)) In blue, the experimental profile with step widths corresponding to the NRA depth resolution. In red, the He profile from SRIM calculations. In dashed green, the damage profile.

3 Results

Results are divided into three parts according to the sample grain sizes (large, medium, and small grain size).

3.1 Large grain size (20-60 µm)

In order to determine an apparent helium diffusion coefficient, helium trapping at grain boundaries had to be minimised. For that purpose, B_4C samples with large grain sizes were ^{3}He implanted: in this material, the grain boundary density is about one hundred times lower than in the medium grain size one. Annealing was performed from 600°C to 800°C (precision ± 10°C) for 1 to 10 h. The helium profiles after annealing are compared to the as-implanted one in Figure 7.

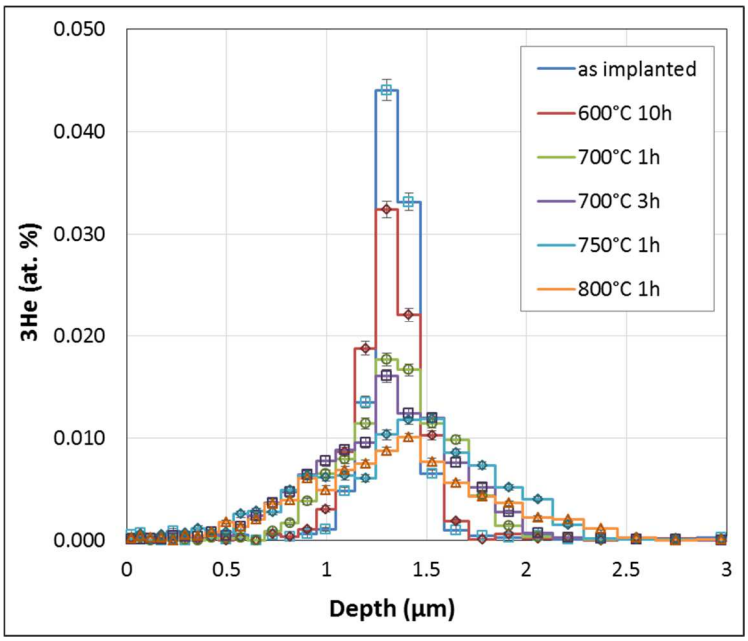

Figure 7: Helium distribution profiles in B_4C (large grains) implanted with 1200 keV ^3He at RT and $2x10^{15}$ at.cm^{-2} and annealed from 600°C to 800°C for 1 to 10h (width of histogram bars: depth resolution; a different sample for each profile).

Figure 7 shows that after annealing the profiles have broadened, which characterises a diffusion process. After heat treatments, the profiles have a complex shape that can be decomposed into two Gaussian curves (e.g. Figure 8) centred at nearly the same depth, giving two distinct contributions:

- A narrow one located at the same depth as the implanted zone, we call Ft in the following. Its width is close to the one in the as-implanted sample, we then assume it corresponds to helium trapped in the implanted zone. In all Gaussian adjustments, the same width as in the non-annealed sample was enforced for this component.
- A broad one we call Fm in the following, we assume corresponding to mobile helium that actually diffused in the material.

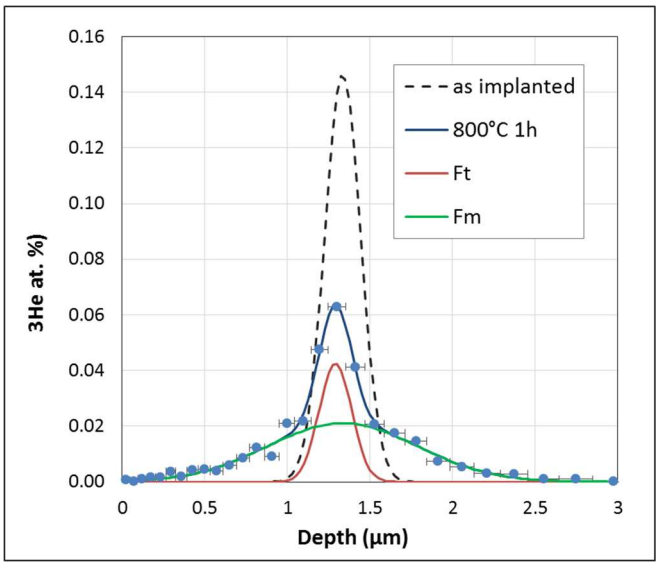

Figure 8: Helium distribution profiles in B_4C (large grains) implanted with 1200 keV ^3He at RT and $2x10^{15}$ at.cm^{-2} and annealed at 800°C for 1h. The profile after annealing is decomposed into two Gaussian curves: in green the "mobile" fraction; in red the "trapped" fraction (horizontal error bars: depth resolution).

In order to analyse helium diffusion, we then considered the sole mobile fraction. In such a large grain material, the helium profiles remain much narrower than the grain size. We then assumed that the grain boundary trapping is negligible so that the helium volume diffusion is not perturbed. In that case, an apparent diffusion coefficient can be derived, first assuming it does not depend on the crystal structure. To calculate a diffusion coefficient, the width of the mobile fraction for each profile was determined from the Gaussian fittings. A consequence of the Fick's law for Gaussian distributions allows writing:

$$\sigma_T^2 = \sigma_0^2 + 2 \cdot D_T \cdot t \qquad \text{(Equation 1)}$$

Where σ_T is the standard deviation of the Gaussian corresponding to the mobile fraction after a heat treatment at a temperature T and a duration t. σ_0 is the standard deviation of the as-implanted profile before annealing (the two σ then include the experimental resolution). D_T is the apparent diffusion coefficient at a temperature T and is defined by:

$$D_T = D_0 \cdot \exp\left(-\frac{E_a}{k \cdot T}\right) \qquad \text{(Equation 2)}$$

With D_0 the pre-exponential factor; E_a the activation energy; k the Boltzmann constant ($8.617x10^{-5}$ eV.K^{-1}).

D_T was calculated for each temperature and duration of annealing (Table 2) and the values were reported into an Arrhenius diagram (Figure 9). In Figure 9, the dots appear relatively aligned; we then deduce that only one diffusion mechanism is active in this temperature range. We then obtain:

- $D_0 = 9x10^{-4} \pm 3x10^{-4}$ cm².s^{-1}.
- $E_a = 2.0 \pm 0.2$ eV.

Table 2. Full widths at half-maximum of the helium profiles and apparent diffusion coefficients as a function of annealing temperature and time.

Annealing temperature (°C)	Annealing time (h)	FWHM (µm)	Apparent diffusion coefficient (10^{-15} cm²/s)
As-implanted	-	0.221	-
600	10	0.419	3.2
700	1	0.675	102
700	3	0.884	61
750	1	1.093	287
800	1	1.146	317

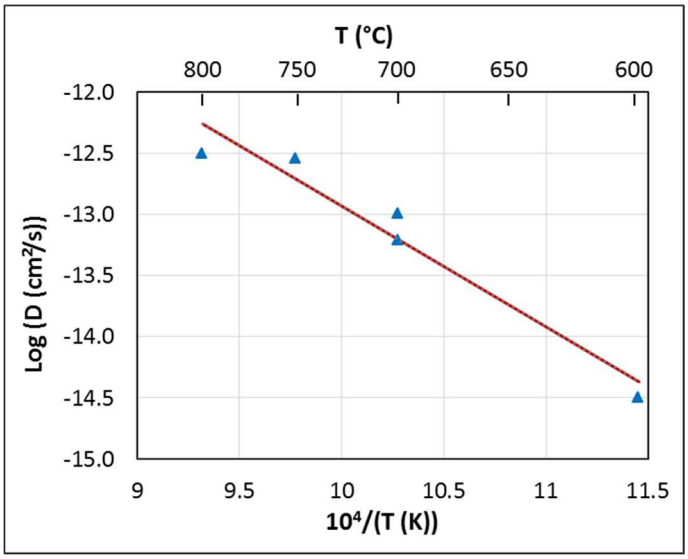

Figure 9: Arrhenius diagram of the apparent diffusion coefficient of helium in boron carbide (large grains)

3.2 Medium grain size (1-6 µm)

B_4C samples were ^{3}He implanted at the same fluence, $2x10^{15}$ at.cm^{-2} (Table 1). The samples were then annealed from 600 to 1000°C for 1 h and analysed by NRA. Helium profiles are shown in Figure 10. We observe that the profile areas are nearly equal whatever the thermal treatment, meaning that most helium remained near the implanted zone. As mentioned above, this means that a longer-range diffusion is negligible.

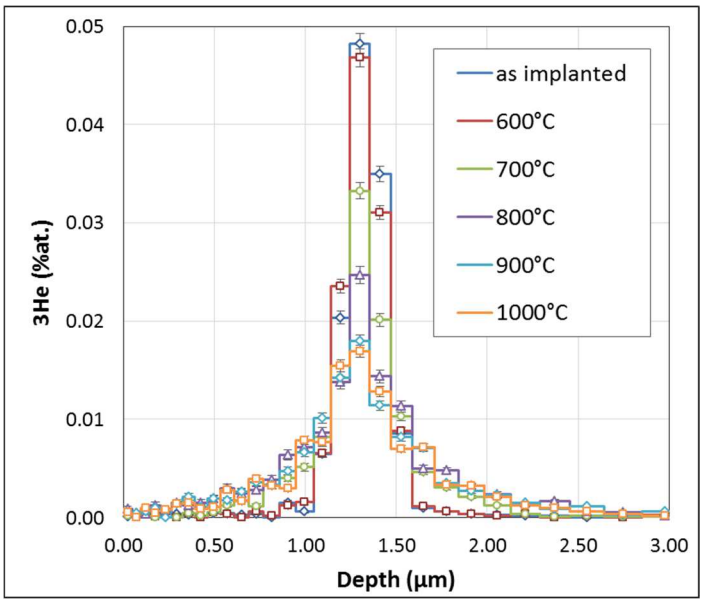

Figure 10: Helium distribution profiles in B_4C implanted with 1200 keV ^3He at RT and 2x10^{15} at.cm^{-2} and annealed up to 1000°C for 1 h (one different sample for each annealing and NRA analysis).

As observed in the large grain size material, the helium profiles broaden from temperatures above 700°C, showing that helium begins to significantly diffuse. However, for temperatures above 800°C and annealing duration of 1 h, the helium profiles do no evolve anymore. Figure 11a gives a better look for high temperature annealing and Figure 11b shows helium profiles in implanted B_4C samples annealed at 800°C for more than 1 h. Note in Figure 11 the two "as implanted" profiles correspond to two different samples. The slight difference we observe corresponds to the experimental reproducibility.

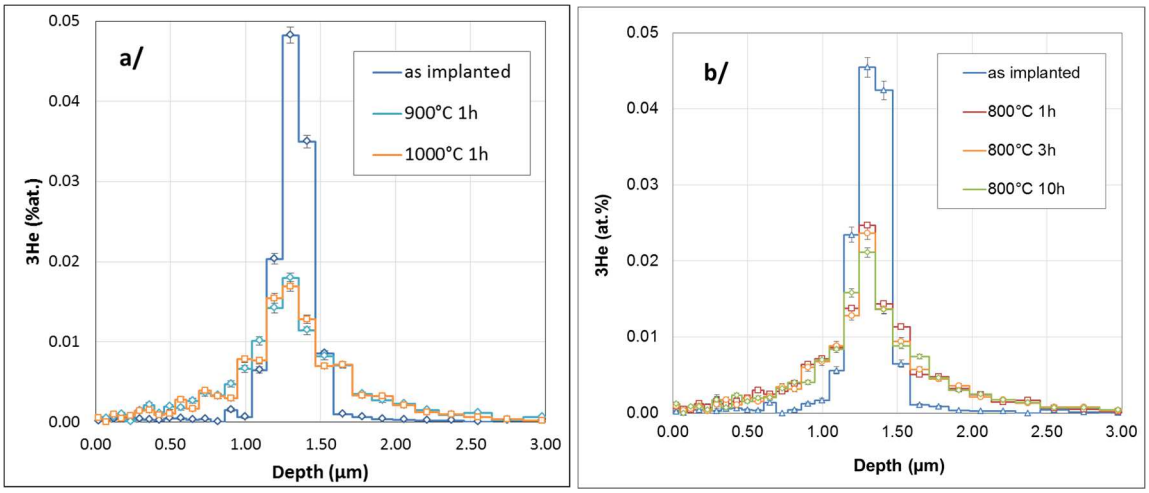

Figure 11: Helium distribution profiles in B_4C implanted with 1200 keV^3He at RT and 2x10^{15} at.cm^{-2}. a: annealed at 900 and 1000°C for 1 h. b: annealed at 800°C for 1, 3 and 10 h. One different sample for each profile.

In Figure 11a, the profiles corresponding to samples annealed at 900°C and 1000°C for 1 h are similar whereas from our calculated diffusion coefficient, the '1000°C-1h' profile should be about twice as wide as the '900°C-1h' one. Figure 11b shows that the samples annealed at 800°C show similar profiles whatever the annealing time between 1 and 10 h. These results clearly show that helium is trapped. Indeed, we have shown in [15] that grain boundaries are very efficient traps for helium and there was no helium diffusion along and across the grain boundaries. This trapping effect could explain why helium profiles remain unchanged for longer time annealing at high temperatures. To check this point, B_4C samples with small grain sizes were studied.

3.3 Small grain size (0.3-1 µm)

B_4C samples with small grain sizes (0.3-1 µm) were implanted with 500 keV ^4He ions at a higher fluence of about 10^{16} at.cm^{-2} (Table 1) in order to allow the formation of clusters. Figure 12 shows TEM images of an implanted sample after a heat treatment at 800°C / 1 h.

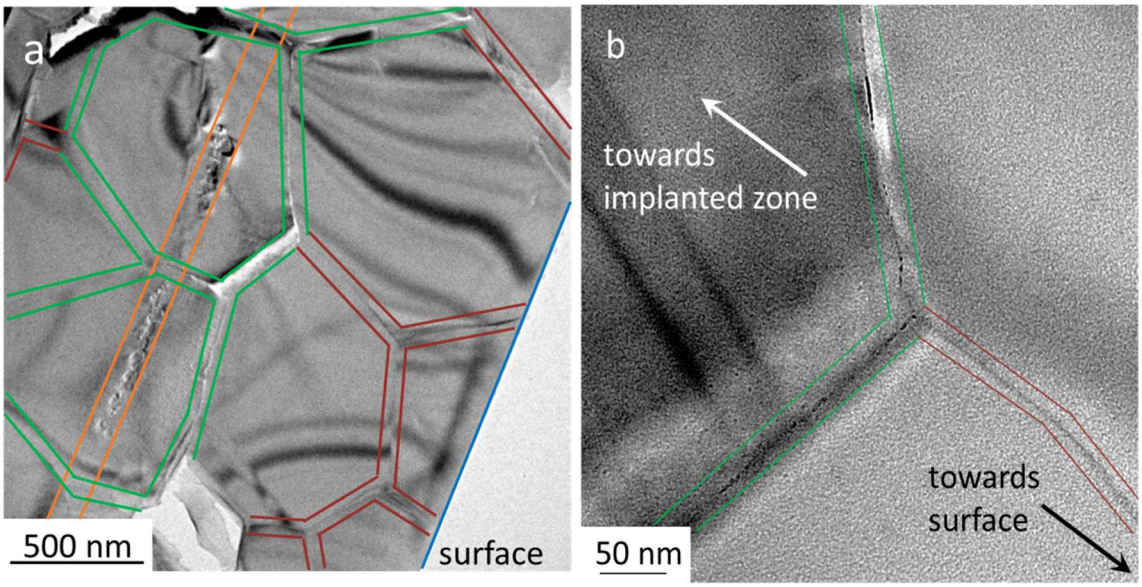

Figure 12: TEM micrographs of B_4C (small grain size) implanted with 500 keV He ions at RT with a fluence of $8x10^{15}$ at.cm^{-2} and annealed at 800°C / 1 h. Orange: implanted zone. Green: grain boundaries that contain bubbles. Red: grain boundaries that do not contain any bubble. a: general view. b: zoom of the centre of a.

Bubbles appear in the grain boundaries (Figure 12a), in agreement with results obtained in [15]. Grain boundaries were distinguished between two types: with bubbles (delimited in green) and without bubbles (in red). Figure 12b presents a triple point where bubbles are visible in the green grain boundaries and not in the red ones. In Figure 12a, we observe that the grain boundaries that contain helium bubbles all surround the implanted zone. This shows that, in those annealing

conditions, there is no helium bubble formation beyond the grain boundaries surrounding the implanted zone.

4 Discussion

4.1 Diffusion at grain boundaries

From the results presented in sections 3.2 and 3.3, it can be concluded that there is no diffusion in and across the grain boundaries, at least up to 1000°C. As already emphasized in [15], this is an important result, which cannot be inferred from experiments on specimens irradiated in reactor. In this latter case, helium is homogeneously produced in the whole material. The trapping effect at the grain boundaries manifests only through the existence of denuded zones in their vicinity, about 30 – 50 nm wide, without helium bubbles. However, evidence of these zones does not mean there is no diffusion through or along grain boundaries. To go further, we analysed helium implanted in the HD20 small grain B_4C after annealing at 800°C for 1 h (in such annealing conditions, we have shown that the helium profile is stabilized in the medium grain size material: Figure 11). In Figure 13, the obtained He profile is compared with the profile obtained in the large grain size material (ERM) in the same annealing conditions.

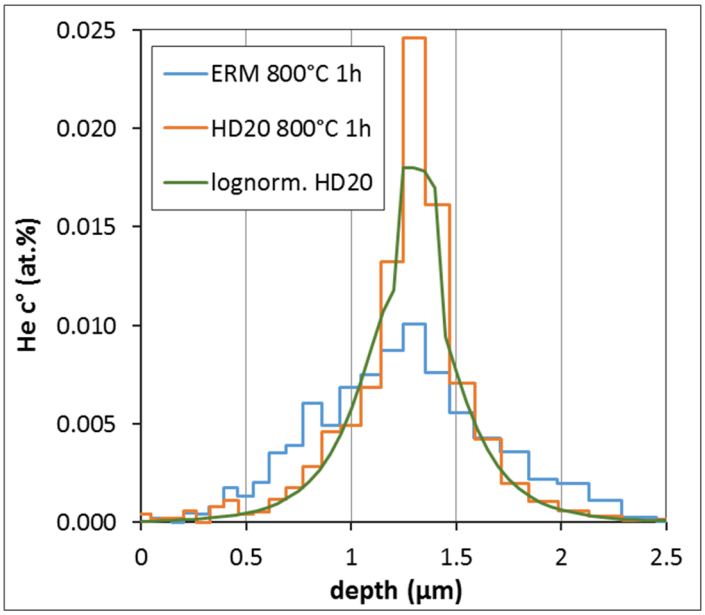

Figure 13: Helium profiles (step-wise curves) obtained with large grain size (ERM, blue curve) and small grain size (HD20, orange curve) materials after annealing at 800°C for 1h (fluence 2.10^{15}/cm²). Superimposed is the distribution of the grain boundaries circling or crossing the implanted zone for the HD20 material (green curve), as deduced from its log-normal grain size distribution.

The HD20 helium profile looks clearly narrower than the ERM one. This means that helium cannot diffuse freely. Here again, the profile looks like constituted by two contributions, the narrow one is located at the depth of the implanted zone. In order to interpret this complex profile; we have considered the distribution of the sole grain boundaries circling or crossing the implanted zone (with a 100 nm width). The metallographic observations of the hot-pressed HD20 material lead to a log-normal grain size distribution (logarithmic variance and median respectively $\sigma = -0.2$; $\mu = 0.6$). From this distribution, we have calculated the density of grain boundaries circling the implanted zone as a function of the distance to the implanted zone or intersecting it. This leads to a bell-shaped curve (figure 13) which closely superimposes to the HD20 helium distribution, excepted in the implanted zone. The distribution of the grain boundaries circling the implanted zone reproduces the broad component of the helium profile; the density of grain boundaries intersecting the implanted zone reproduces only partially the narrow component of the helium profile. It follows that at the helium fluence here chosen, helium trapping (e.g. in clusters) in the implanted zone or into the grains is actually low (see section 4.2): there is almost no helium outside the grain boundaries. Finally, due to a much higher density of grain boundaries in the HD20 material, the trapped fraction in the implanted zone is much higher than in the ERM material. Thus, we can assume that, as soon as annealing has been processed for sufficient time and temperature conditions (see also Figure 11), the low-concentration implanted helium profiles in boron carbide with small or medium grain sizes fit the distribution of the grain boundaries circling the implanted zone. There however remains a small fraction trapped in the implanted zone. This confirms helium does not diffuse through or in the grain boundaries in the temperature range we consider here.

In our previous papers [15,31] helium behaviour at high temperatures was followed by TEM. After annealing at 1200°C, small helium bubbles were observed near triple grain boundaries, pointing outside the implanted zone, as shown in Figure 14. This means that in this temperature range, helium can either diffuse in the grain boundaries or evaporate from the bubbles into the material and then re-condense in the vicinity of the grain boundaries. In addition, at 1500°C, the grain boundaries can be opened, this meaning growth and interconnection of the intergranular bubbles.

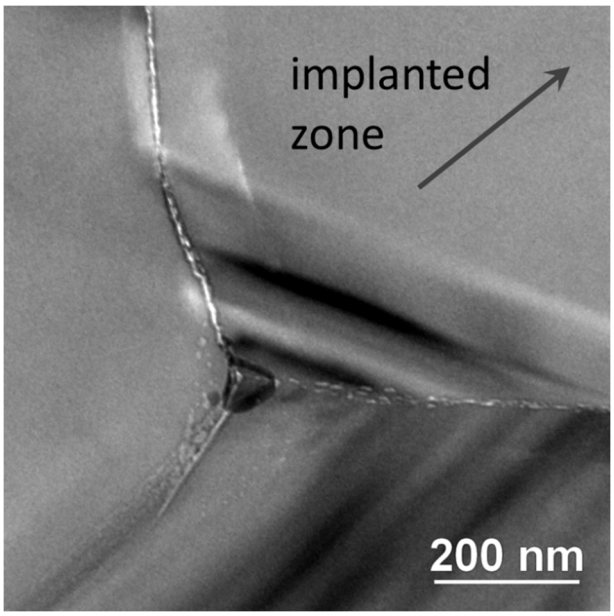

Figure 14. Helium bubbles in grain boundaries pointing outside the implanted zone (mean grain size material). After annealing at 1200°C for 1 h, bubbles can be seen in the bottom left grain boundary, while the implanted zone is towards the upper right corner (arrow).

4.2 Helium distribution

The ^{3}He implantations were performed at helium concentrations close but lower than the bubble formation threshold determined by TEM [15], in order to favour the mobile fraction. However, the helium distributions present two superimposed Gaussian-like components, both centred close to the implantation maximum. For the low and medium grain size materials, the so-called trapped component mainly corresponds to helium precipitated into the grain boundaries, as calculated in section 4.1, leading to the He bubbles free zone observed by TEM (denuded zones), about 30 to 50 nm large. Nevertheless, for the large grain size material, the grain boundary density is about 100 times lower than in the mean grain size material; this trapped component should then be considered as negligible. As a result, we have to assume that in the implanted zone, a small fraction of helium is trapped even if bubbles are still not visible. Apart from few bubbles, the trapped species cannot here be identified. Either they form helium clusters too small to be observed by TEM, or they form low mobile helium-defect complexes since about 40 atoms are displaced by each implanted helium atom (SRIM estimation), with the damage profile nearly superimposed to the helium profile (Figure 6).

4.3 Diffusion coefficient and activation energy

As mentioned in section 3.2, the helium concentration had to be high enough so that we could determine the profiles with a good resolution in a reasonable experimental time. A 2×10^{15} cm^{-2}

fluence was chosen, leading to a maximum implanted concentration of about 10^{20} cm^{-3}. This value appears close to the cluster formation threshold. In Figure 5, no helium clusters are visible. As mentioned above, this however cannot preclude the formation of helium-defect complexes. On the other hand, in such a rhombohedral structure, an anisotropic diffusion cannot be excluded (see here-below), that the sintered, non-textured microstructure of the samples would hide.

In a preliminary work [31], an apparent diffusion coefficient had already been estimated and activation energy of 0.52 eV was derived, strongly different from the present result. This can be explained by the depth resolution and the yield of this seminal experiment, too low to allow evidencing the two components we observed here.

The apparent diffusion coefficients estimated in the present study are quite different (about 2 decades higher) from the ones published by Clayton [18] and Hollenberg [19] (Figure 15). As mentioned in the introduction, such a difference can tentatively be explained. Clayton and Hollenberg performed helium desorption experiments on materials irradiated in reactor. As a result, the diffusion coefficient deduced from those experiments possibly recovers different mechanisms such as helium-defect complexes migration, trapping and detrapping from the helium bubbles, interactions with grain boundaries, surface desorption, porosity degassing, and so on. Moreover, helium diffusion occurs in a material with a modified composition (boron burning, lithium formation) and with different defect configurations (defect creation by neutron scattering in a fast neutron spectrum is about six times higher than by the sole He slowing-down [16]). The D values determined in the present study are certainly less biased by such effects. This suggests the lower the defects density the faster the helium diffusion. This could be checked by performing infusion then desorption experiments.

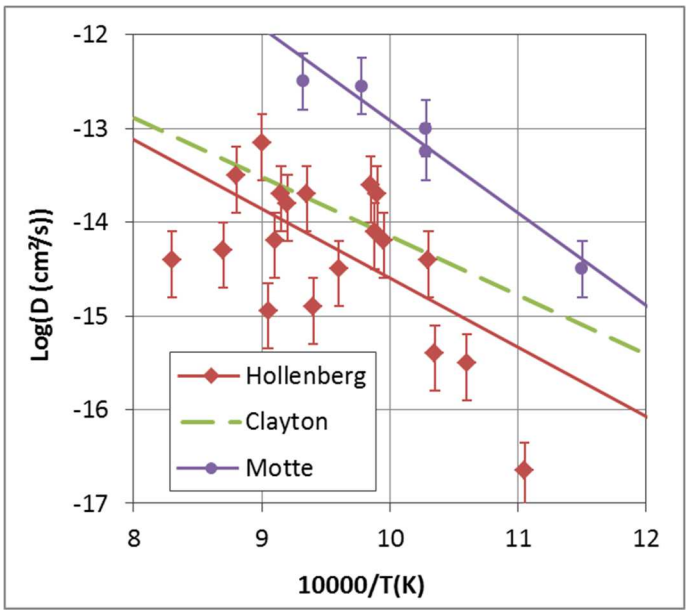

Figure 15. Helium diffusion coefficients in boron carbide. Clayton [18] and Hollenberg [19]: helium produced by neutron irradiation, analyses performed by desorption. Motte (this study): implanted helium, NRA profiling.

The ab -initio calculations performed by A. Schneider and co-workers lead to two activation energies: 1.2 eV for a 2D diffusion along the (111) planes and 2.2 eV for a 3D diffusion [24]. Those values are very close to those obtained by Kovyrshin [20] who irradiated boron carbide powders and who identified two release steps by thermo-desorption. The activation energy we determined here is close to the higher one; that is for a 3D diffusion. EBSD (Electron Back-Scattered Diffraction) observations (not presented in this paper, see [32]) have evidenced that the materials of the present study are nearly isotropic, with no noticeable texture. Figure 16 illustrates the difference between the actual diffusion length along the (111) direction and the apparent one towards the surface or the bulk. Integrating this effect along all possible (111) orientations in the material would lower the apparent diffusion lengths and distort the helium profile. This does lead to lower the apparent activation energy, but still far from the 1.2 eV value calculated by Schneider *et al*.

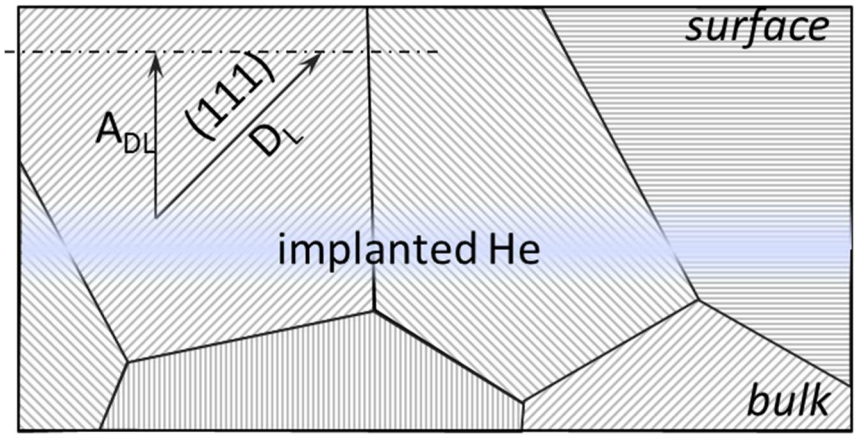

Figure 16: 2D diffusion along the (111) planes. D_L: diffusion length along the plane for given annealing conditions. A_{DL}: apparent diffusion length from the helium layer.

A 2D diffusion, associated to low activation energy, should then be visible, for example with large wings on both sides of the diffusion profiles. Part of them could be hidden in the background noise. However, as mentioned above, the He content measurement by NRA corresponds to the implanted fluence, so this masked long-range diffusion should be very weak. Mechanisms able to inhibit this 2D diffusion should be then identified. As already mentioned, helium implantation creates a high density of defects, very close to the implanted helium zone (cf. Figure 6; note that this defects to helium ratio would be similar in a thermal neutron flux but about 6 times higher in a fast neutron flux [16]). They could prevent migration along the (111) planes or lead to the formation of helium – defect complexes with a higher diffusion energy similar to the 3D value. At last, the micrographs of the samples show twin boundaries: in that case, the free diffusion along the (111) planes cannot take place anymore. Either He is trapped at the twin boundaries or the diffusion paths make zig-zags. Those defects are always present in B_4C crystals, which density depends on the elaboration process and the stoichiometry [33]: this effect should be analysed. On the other hand, in-progress studies show that most defects induced by ion implantation are not stable at 500°C [6,7]. The role of the implantation defects could then be evaluated by performing the ^{3}He implantation at 500°C (note that the profile broadening would be negligible).

4.4 Diffusion lengths

From the apparent diffusion coefficient values, it is possible to estimate the diffusion lengths for different annealing temperatures and durations (Figure 17). The diffusion lengths are very low at 500°C. At higher temperatures, the diffusion lengths are much larger. For example, after a 800°C/10h annealing, helium can diffuse up to 5 µm, which is larger than the medium grain size of this study, thus large enough for helium to encounter grain boundaries and create the bubble walls as observed

in [15, 34]. Extrapolating those values to the irradiation performed in fast neutron reactors (that is for about one year in the temperature range 500 – 1000°C) lead to sub-millimetric diffusion lengths. Those distances are comparable to the separation lengths of the microcracks forming under irradiation. Free helium should then escape through the microcrack network as soon as it forms: this release acceleration is clearly observed in [19]. However, the retention rates below this cracking threshold (burnup about $5x10^{21}$ neutron captures per cm^3) are high [12], meaning the trapping mechanisms (helium bubbles in the grain boundaries and in the grains) are very efficient.

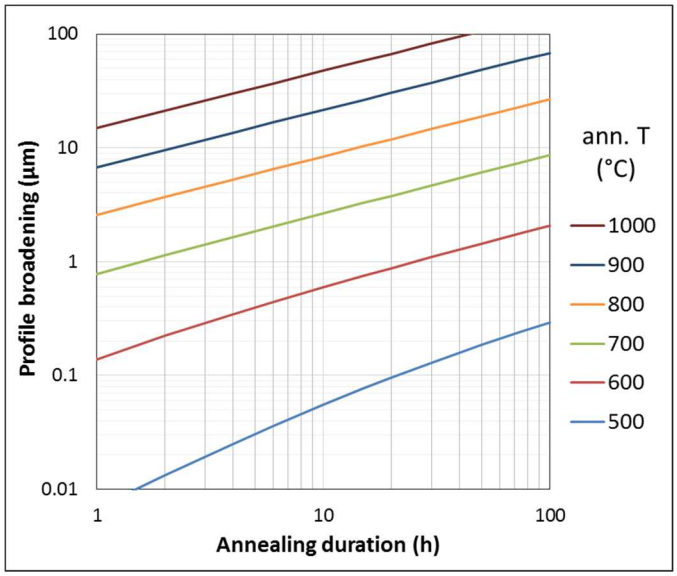

Figure 17: Diffusion lengths of helium in boron carbide estimated from the apparent diffusion coefficient, depending on the temperature and duration of annealing.

5 Conclusion

Results presented in this paper contribute to a better understanding of helium diffusion in B_4C and of the influence of the initial microstructure. They are complementary of results dealing with helium cluster nucleation and growth [15]. Moreover, all those results are obtained in materials with a relatively low defect concentration: this allows a comparison with neutron irradiated materials then an estimation of the induced specific effects, such as helium clusters, composition variation (boron burning and lithium formation) or ballistic damage induced by fast neutron scattering.

NRA analyses of helium-implanted then annealed B_4C samples were performed. It was shown that the helium profiles obtained in B_4C with a large grain size broadened with increasing temperature and annealing duration, meaning that diffusion occurred. However, in the case of medium grain size samples, above 800°C, or for durations longer than 1h at those same temperatures, the profile

widths remain constant. At last, comparing the grain size distribution with the implanted helium profiles of boron carbide with small grain size, allowed us concluding that in those conditions helium is trapped in the grain boundaries. There is no helium diffusion along and across the grain boundaries for temperatures at least up to 1000°C, in agreement with the assumptions we made in [15].

To minimize grain boundary trapping, helium was implanted in large grain size B_4C. From the evolution of the profile widths between 600 and 800°C, an apparent diffusion coefficient was evaluated, with activation energy of 1.96 ± 0.2 eV. Unlike ab-initio calculations, only one diffusion mechanism is observed, corresponding to the ab-initio isotropic diffusion: the low energy, anisotropic diffusion along the (111) planes is not observed, possibly hidden by the formation of helium-defect complexes or interactions with the twin boundaries.

Further studies, such as desorption or infusion experiments could be performed to improve the understanding of the diffusion mechanisms and obtain a more accurate value of the helium apparent diffusion coefficient. Such experiments should be performed on monocrystals, which are unfortunately not available. Ab-initio calculations are also in progress to study the behaviour of several helium atoms in a damaged B_4C matrix and the influence of charged point defects [35].

6 Acknowledgments

The experiments at the CEMHTI laboratory have been performed in the frame of the CEA-CNRS NEEDS collaboration contract. We are very grateful to our colleagues of IRCER (Limoges University, France) who prepared the small grain size material by hot-pressing. The FIB equipment was partly financed thanks to the French GENESIS ANR project.

7 References

[1] D. Gosset, Absorber materials for Generation IV reactors, in “Structural Materials for Generation IV Nuclear Reactors”, 1st Ed., ch. 15, P. Yvon ed., ISBN 9780081009123, Elsevier (2016)

[2] V. Domnich, S. Reynaud, R. A. Haber, and M. Chhowalla, “Boron Carbide: Structure, Properties, and Stability under Stress,” *J. Am. Ceram. Soc.*, vol. 94, no. 11, pp. 3605–3628, Nov. 2011.

[3] F. Thévenot, “Boron carbide—A comprehensive review,” *J. Eur. Ceram. Soc.*, vol. 6, no. 4, pp. 205–225, Jan. 1990

[4] D. Gosset, “Neutron Absorber Materials,” in *Handbook of Nuclear Engineering*, Dan Gabriel Cacuci., 2010.

[5] D. Gosset, S. Miro, S. Doriot, G. Victor, and V. Motte, “Evidence of amorphisation of B_4C boron carbide under slow, heavy ion irradiation,” *Nucl. Instr. and Methods in Phys. Res. Sect. B Beam Interact. Mater* , Aug. 2015

[6] D. Gosset, S. Miro, S. Doriot, and N. Moncoffre, “Amorphisation of boron carbide under slow heavy ion irradiation,” *J. Nucl. Mater.*, vol. 476, pp. 198–204, Aug. 2016

[7] G. Victor, Y. Pipon, N. Bérerd, N. Toulhoat, N. Moncoffre, N. Djourelov, S. Miro, J. Baillet, N. Pradeilles, O. Rapaud, A. Maître, and D. Gosset, "Structural modifications induced by ion irradiation and temperature in boron carbide B_4C," *Nucl. Instrum. Methods Phys. Res. Sect. B Beam Interact. Mater. At.*, vol. 365, pp. 30–34, Dec. 2015.

[8] A. Jostsons, C. K. H. DuBose, G. Copeland, and J. O. Stiegler, "Defect structure of neutron irradiated boron carbide," *J. Nucl.Mater.*, vol. 49, no. 2, pp. 136–150, Dec. 1973.

[9] A. Jostsons and C. K. H. Dubose, "Microstructure of boron carbide after fast neutron irradiation," *J. Nucl.Mater.*, vol. 44, no. 1, pp. 91–95, Jul. 1972.

[10] V. N. Bykov, V. A. Rudenko, V. P. Tarasikov, and V. I. Shcherbak, "Effect of high temperature annealings on swelling and helium release in boron carbide irradiated with neutrons," *INIS-SU--112*, 1988.

[11] V. I. Shcherbak, V. N. Bykov, V. P. Tarasikov, and V. A. Rudenko, "Radiation damage in neutron irradiated boron carbide," *At. Energiya*, vol. 60, pp. 227–230, 1986.

[12] G. W. Hollenberg, J. .Jackson, and J. A. Basmajian, "In-reactor measurement of neutron absorber performance," *Nucl. Technol.*, vol. 49, pp. 92–101, 1980.

[13] G. G. W. Hollenberg, B. Mastel, and J. A. Basmajian, "Effect of irradiation temperature on the growth of helium bubbles in boron carbide," *J. Am. Ceram.Soc.*, vol. 63, pp. 376–380, 1979

[14] T. Stoto, N. Housseau, L. Zuppiroli, and B. Kryger, "Swelling and microcracking of boron carbide subjected to fast neutron irradiations," *J. Appl. Phys.*, vol. 68, no. 7, p. 3198, 1990.

[15] V. Motte, D. Gosset, G. Gutierrez, and N. Moncoffre, "Helium clusters nucleation and growth in implanted B_4C boron carbide", J. Nucl. Mater. **514** (2019) 334-347

[16] D. Gosset and P. Herter, Evaluation of damage in neutron irradiated boron carbide, Nucl. Instr. Meth. B-**434** (2018) 66-72

[17] Y. You, K. Yoshida, T. Inoue and T. Yano, Helium bubbles and trace of lithium in B_4C control rod pellets used in JOYO experimental fast reactor, J. Nucl. Sci. Tech., 55:56, 640-648 (2018)

[18] J. C. Clayton, W. A. Bostrom, and F. C. Schrag, "The release of helium from slightly irradiated boron carbide and boron carbide-silicon carbide plates," *WAPD-255*, 1962.

[19] G.W. Hollenberg, Helium diffusion in irradiated boron carbide, HEDL-SA-2236-FP (1981)

[20] V.G. Kovyrshin, Liberation of helium in the heating of irradiated boron carbide, At. Energ.,**53-2**, 112-113, (1982)

[21] V.V. Svetukhin, Determining the Energy Parametersof the Helium Accumulation Centersin Irradiated Boron Carbide from Thermodesorption Spectra, Tech. Phys. Lett.,**29-2** (2003) 154–156

[22] Y. You, K. Yoshida and T. Yano, First-principles investigation of neutron-irradiation induced point defects in B4C, a neutron absorber for sodium-cooled fast nuclear reactors, Jpn. J. Appl. Phys. **57** (2018) 055801

[23] D. Gosset, B. Kryger, J.P. Bonal, C. Verdeau and K. Froment, Evolution of thermo-physical properties and annealing of fast neutron irradiated boron carbide, J. Nucl. Mater. **500** (2018) 166e175

[24] A. Schneider, G. Roma, J.-P.Crocombette, D. Gosset, and V. Motte, "Stability and kinetics of helium interstitials in boron carbide from first principles," *J. Nucl.Mater.*, vol. 496, pp. 157–162, 2017.

[25] T. Sauvage, H. Erramli, S. Guilbert, L. Vincent, M.-F. Barthe, P. Desgardin, G. Blondiaux, C. Corbel, J.P. Piron, F. Labohm and A. Van Veen, Profile measurements of helium implanted in UO2sintered pellets by using the $^3He(d, \alpha)^1H$ nuclear reaction analysis technique, J. Nucl. Mater, 327 (2004) 159-164

[26] P. Trocellier, S. Agarwal, S. Miro, S. Vaubaillon, F. Leprêtre and Y. Serruys, IBA studies of helium mobility in nuclear materials revisited, J. Nucl. Mater, 467-1, 68-81 (2015)

[27] F. Chamssedine, T. Sauvage, and S. Peuget, "DIADDHEM set-up: New IBA facility for studying the helium behavior in nuclear glasses," *NIM-B,* 268-11–12, 1862–1866 (2010).

[28] L. Beck, Y. Serruys, S. Miro, P. Trocellier, E. Bordas, F. Leprêtre, D. Brimbal, Th. Loussouarn, and H. MartinIon "irradiation and radiation effect characterization at the JANNUS-Saclay triple beam facility", J. Mater. Res., 30-9, 1183-1194 (2015)

[29] J. F. Ziegler, "SRIM - The Stopping and Range of Ions in Matter", www.srim.org

[30] G. Martin, T. Sauvage, P. Desgardin, P. Garcia, G. Carlot, and M. F. Barthe, "Accurate automated non-resonant NRA depth profiling: Application to the low 3He concentration detection in UO2 and SiC," *NIM-B.*,258-2,471–478 (2007).

[31] V. Motte, D. Gosset, S. Miro, S. Doriot, S. Surblé, and N. Moncoffre, “Helium behaviour in implanted boron carbide,” *EPJ Nucl. Sci. Technol.*, vol. 1, p. 16, 2015.

[32] V. Motte, Behavior of helium implanted in B_4C boron carbide, thesis, Lyon-1 University, France, (2017)

[33] K.Y. Xie, Qi An, M.F. Toksoy, J.W. McCauley, R.A. Haber,W.A. Goddard III, and K.J. Hemker, Atomic-Level Understanding of “Asymmetric Twins” in Boron Carbide, PRL 115, 175501 (2015)

[34] T. Stoto, J. Ardonceau, L. Zuppiroli, M. Castiglioni, and B. Weckermann, “Behaviour of implanted helium in boron carbide in the temperature range 750 to 1720°C,” *Radiat. Eff.*, vol. 105, no. 1–2, pp. 17–30, Dec. 1987.

[35] K. Gillet, G. Roma, J.P. Crocombette and D. Gosset, The influence of irradiation induced vacancies on the mobility of helium in boron carbide, J. Nucl. Mater. **512** (2018) 288-296